Available online at www.sciencedirect.com
SCIENCE DIRECT®
Pergamon
Acta Materialia 51 (2003) 2933–2957
Acta MATERIALIA
www.actamat-journals.com

Resistance-curve and fracture behavior of Ti–Al_3Ti metallic–intermetallic laminate (MIL) composites

Aashish Rohatgi [a,*], David J. Harach [b], Kenneth S. Vecchio [a], Kenneth P. Harvey [a]

[a] *University of California, San Diego, Department of Mechanical and Aerospace Engineering, Materials Science and Engineering Group, La Jolla, CA 92093-0411, USA*
[b] *Materials Engineering Laboratory, Building 469, PO Box 357058, San Diego, CA 92135-7058, USA*

Received 7 October 2002; accepted 27 January 2003

Abstract

The R-curve and fracture toughness behavior of single-edge notch beams of Ti–Al_3Ti metallic–intermetallic laminate (MIL) composites has been investigated. Composites with 14, 20, and 35% volume fraction Ti, with a corresponding intermetallic layer thickness of ~540, ~440, and ~300 microns, respectively, were tested in crack arrester and crack divider orientations. In the arrester orientation, the R-curve could not be determined for the two highest Ti volume fraction compositions as the main crack could not be grown through the test samples. In the divider orientation, R-curves were determined for all three Ti volume fractions tested. The laminate composites were found to exhibit more than an order of magnitude improvement in fracture toughness over monolithic Al_3Ti. Crack bridging and crack deflection by the Ti layers were primarily responsible for the large-scale bridging conditions leading to the R-curve behavior and enhanced fracture toughness. Estimates of steady-state toughness under small-scale bridging conditions were in close agreement with experimental results.

Keywords: Bending test; Toughness; Titanium aluminide; Multilayers; Fracture

1. Introduction

1.1. Ti–Al_3Ti laminate composites

Titanium–titanium tri-aluminide (Ti–Al_3Ti) metallic–intermetallic laminate (MIL) composites have been produced from elemental titanium and aluminum foils by a novel one-step process utilizing a controlled reaction at elevated temperature and pressure [1]. The novelty of this fabrication process lies in the fact that it is performed in open air and produces a fully dense laminate composite. The thickness of the original titanium and aluminum foils is chosen to ensure that the entire aluminum layer is consumed upon reaction with the adjacent titanium layers. Such a layering scheme results in a composite with alternate layers of Al_3Ti and

* Corresponding author. Tel.: +1-858-534-7888; fax: +1-858-834-5698.
E-mail address: arohatgi@ucsd.edu (A. Rohatgi).

1359-6454/03/$30.00
doi:10.1016/S1359-6454(03)00108-3

residual Ti, and the thickness of the final layers are dependent upon the thickness of the original Ti and Al foils. The above process is highly flexible since metal/alloy foils other than Ti can be used individually, or in combination, within the same composite, to produce their respective metal–metal aluminide composites. For example, MIL composites using Fe-based, Ni-based, and Co-based alloys as the starting metal layer (instead of Ti) have been successfully fabricated using the above technique [1].

Of the various possible aluminides in the Ti–Al system, the formation of the intermetallic Al_3Ti is thermodynamically and kinetically favored over the formation of other aluminides when reacting Al directly with Ti. This preferential formation of Al_3Ti is fortuitous as its Young's modulus (216 GPa) and oxidation resistance are higher, and the density (3.3 g/cm^3) lower than that of the other titanium aluminides such as Ti_3Al and TiAl [2]. The high compressive strength and high compressive stiffness of Al_3Ti (or intermetallics, in general) results from their high bond strength. However, intermetallics are brittle at low temperatures due to the limited mobility of dislocations (and paired superdislocations with anti-phase boundaries), insufficient number of slip or twinning systems, and/or very low surface energy resulting in little to no plastic deformation at the crack tip. For example, Al_3Ti is extremely brittle at room temperature and has a very low fracture toughness of ~2 MPa$\sqrt{m}$ [3]. Various investigators have tried to improve the toughness of intermetallics [4,5] by reinforcing them with particles [6–8], rods [9–12], or layers of ductile metals [4,13–19]. It is interesting to note that for the same volume fraction of the ductile reinforcing phase, the ductile phase in laminate form has the maximum toughening efficiency followed by fiber and particulate morphology, in that order [8,20]. In the laminate composites fabricated in this research, the ductile metal phase is alternated with the brittle intermetallic phase instead of being used as a reinforcement for the bulk intermetallic.

The concept of creating laminate composites to enhance the toughness of materials is not new. In fact, as early as 1966, laminates of a Ti–5Al–2.5Sn alloy have been shown to exhibit six to seven times higher toughness than a bulk sample of the same thickness [21]. The various toughening mechanisms responsible for the higher toughness of the laminates are described in the next section. Table 1 summarizes the fracture toughness and stiffness of various ductile–brittle material systems in the literature. The fracture toughness and stiffness of the composites in Table 1 are normalized by their respective densities to compare the various material combinations on a weight basis. The specific modulus of the laminates is seen to vary approximately two orders of magnitudes from ~10^6–10^8 m^2/s^2, while the specific initiation fracture toughness generally ranges from 10^{-4} to a few 10^{-3} m$^2\sqrt{m}$/s^2. Among the laminates listed from the literature, the diffusion bonded laminates of Al and Al_2O_3 possess the highest specific initiation fracture toughness of ~60×10^{-4} m$^2\sqrt{m}$/s^2 and a corresponding specific modulus of ~4×10^7 m^2/s^2 at a large volume fraction (~0.8) of the ductile phase (Al). Such a large specific fracture toughness of 80%Al–20%Al_2O_3 composites is not surprising considering that the composite is predominantly a ductile metallic phase. On the other hand, the γ-TiAl–TiNb composites have ~30% lower specific initiation fracture toughness of ~40×10^{-4} m$^2\sqrt{m}$/s^2 and a similar specific modulus as the Al–Al_2O_3 system, but at a much lower volume fraction (~0.1–0.2) of the ductile phase (TiNb) [15,22]. In other examples, metal–Al_2O_3 composites, where the metal may be Cu [16,23], Ni [23], or Al [11,16,19,23], have a substantially higher specific modulus of ~7-10×10^7 m^2/s^2 with a mediocre specific initiation fracture toughness of ~10-30×10^{-4} m$^2\sqrt{m}$/s^2. The high specific modulus of the metal–Al_2O_3 systems is due to the high (415 GPa) modulus of the Al_2O_3 phase. Thus, Table 1 serves to show that a laminate geometry is a very useful way to "mix-n-match" various materials to come up with material-systems with the desired modulus and fracture toughness.

The overall aim of this research was to create a material with high specific strength, toughness, and stiffness for lightweight armor and high performance structural applications. While monolithic titanium is currently being actively used in armor [24–27], and structural applications, high production costs limit its widespread use. As will be

Table 1
Summary of earlier work on fracture mechanics in ductile (metal)–brittle (ceramic/intermetallic) composite materials. The entries are arranged in the order of increasing specific modulus.

Material system (Density (Kg/m^3), Young's Modulus (GPa))	Characteristic dimensions	Volume fraction	Calc. density kg/m^3	Calc. modulus GPa	Specific modulus 10^7 m^2/s^2	Fracture toughness (MPa√m) and sample dimensions (mm)	Specific K (10^{-4} $m^2\sqrt{m}/s^2$)	Reference
PMMA matrix (1200[a], 3[A]) & [D]Al wires (2700[b], 70[A])	Al dia.=510 μm	Al: 0.028	1242	5	0.4	K_0= 1^{CT} 25-64×5.5–9.3×12, LSB	8.1	[11]
Microlaminates of Nb (8570[b], 105[A]) or Nb alloy and intermetallic Cr_2Nb (7660[k], 218[k])	Thickness of each=2 μm	Nb: 0.5	8115	162	2	K_0= $4–5^{3P\text{-}CD}$ K_{ss}=12–14 25.4×8×0.130, LSB	$4.9–6.2^{CD}$ 14.8–17.3	[17]
	6 μm					K_0=$4–5^{3P\text{-}CD}$ K_{ss}=20 25.4×8×0.132, LSB	$4.9–6.2^{CD}$ 24.7	
Microlaminates of Nb (8570[b], 105[A]) or Nb alloy and intermetallic Nb_3Al (7290[j], 236[j])	Thickness of each=2 μm	Nb: 0.5	7930	171	2.2	K_0=$4–5^{3P\text{-}CD}$ K_{ss}=10–11 25.4×8×0.130, LSB	$5–6.3^{CD}$ 12.6–13.9	[17]
Microlaminates of Nb (8570[b], 105[A]) or Nb alloy and intermetallic $(Nb,Ti)_3Al$ (7290[j], 236[j])	Thickness of each=2 μm	Nb: 0.5	7930	171	2.2	K_0= $4–5^{3P\text{-}CD}$ K_{ss}=12–14 25.4×8×0.130, LSB	$5–6.3^{CD}$ 15.1–17.7	[17]
Nb_3Al (7290[j], 236[j])& Nb/Nb_2Al particles in a $NbAl_3$ (4550[m], 120[E]) matrix	Particle size: 10–20 μm	$NbAl_3$: 0.78–0.93	5153–4742	146–128	2.8–2.7	K_{IC}=$3.5^{SEB\text{-}3P}$, 24×5×3	6.8–7.4	[37]
Nb (8570[b], 105[A]) filaments in $NbAl_3$ (4550[m], 120[E]) matrix	Fiber dia.: 250 μm	Nb: 0.20	5354	117	2.2	K_{IC}=$9.6^{SEB\text{-}3P}$, 24×5×3	17.9	

(*continued on next page*)

Table 1 (*continued*)

Material system (Density (Kg/m^3), Young's Modulus (GPa))	Characteristic dimensions	Volume fraction	Calc. density kg/m^3	Calc. modulus GPa	Specific modulus 10^7 m^2/s^2	Fracture toughness (MPa√m) and sample dimensions (mm)	Specific K (10^{-4} m^2√m/s^2)	Reference
Laminates of ^{D}Nb (8570^{b}, 105^{A}) & Nb_3Al (7290^{j}, 236^{j})	Nb: 40 μm	Nb: 0.16	7495	215	2.9	K_0=4.8$^{DC(T)-CD}$, ∅×33×2.8, LSB	6.4 ^{CD}	[34]
	Nb: 40 μm	Nb: 0.16	7495	215	2.9	K_0=7.3^{SEB-CA}, Span 35–40×9.3×3.5, LSB	9.7 ^{CA}	
	Nb: 95 μm	Nb: 0.15	7482	216	2.9	K_0=6.7$^{DC(T)-CD}$, ∅×33×3.5–3.6, LSB	9 ^{CD}	
	Nb: 85 μm	Nb: 0.14	7469	218	2.9	K_0=9^{SEB-CA}, Span 35–40×12.5×3.5, LSB	9.5 ^{CA}	
	Nb: 218 μm	Nb: 0.17	7508	214	2.8	K_0=7.1$^{DC(T)-CD}$, ∅×33×3.5–3.6, LSB	9.5 ^{CD}	
	Nb: 218 μm	Nb: 0.17	7508	214	2.8	K_0=10.4^{SEB-CA}, Span 35–40×13.3×3.6, LSB	13.9 ^{CA}	
WC (15630^{l}, 534^{A}) grains in a ^{D}Co (8860^{b}, 183^{C}) /Co-alloy matrix	WC: 0.6–2.2 μm	Co: 0.1–0.25	14953–13938	499–446	3.3–3.2	K_{IC}=11–17$^{SEB/3P}$,32×6×2	7.4–12.2	[38]
Laminates comprising γ-TiAl (Ti-31 wt% Al) (3700-3900^{g}, 170^{g}) and ^{D}TiNb (5700^{h}, 62^{h})	TiNb thickness=150 μm	TiNb: 0.22	4140–4296	146	~3.5	K_0=8^{3P-CD} & 20^{3P-CA} L×15×B,LSB	18.6–19.3 ^{CD} 46.6–48.3 ^{CA}	[22]
Eutectic and hypereutectic NiAl+Mo system, fibrous dispersion of Mo (10200^{b}, 325^{D})in NiAl (5900^{n}, 235^{n}) matrix	Mo dia.<1 μm	Mo: 0.12	6416	246	3.8	K_{IC}=9 $^{SEB-3P}$	14	[39]
		Mo: 0.16	6588	249	3.8	K_{IC}=14 $^{SEB-3P}$ 28.6×7.6×6.4	21.3	
γ-TiAl (Ti-50.5 at.% Al) (3700-3900^{g}, 174^{g}) matrix with ^{D}γ-TiNb (Ti-33 at.% Nb) (5700^{h}, 62^{h}) discs	β-TiNb dia.=500 μm, thickness=50 μm	β-TiNb: 0.10	3900–4080	~163	4.2–4	K_0=16.3^{3P-CD} & 14.3^{3P-CA}, Span 60×15×2.5, LSB	40–41.8 ^{CD} 35.1–36.7 ^{CA}	[15]

(*continued on next page*)

Table 1 (*continued*)

Material system (Density (Kg/m^3), Young's Modulus (GPa))	Characteristic dimensions	Volume fraction	Calc. density kg/m^3	Calc. modulus GPa	Specific modulus 10^7 m^2/s^2	Fracture toughness (MPa$\sqrt{m}$) and sample dimensions (mm)	Specific K (10^{-4} m$^2\sqrt{m}$/s^2)	Reference
Laminates of ^{D}Ti (4500^{b}, 116^{A}) & Al_3Ti (3300^{o}, 216^{o})	Ti Thickness:	Ti:						Current Work
	158 μm	0.35	3720	181	4.9	K_0=62$^{SEB\text{-}3P/CD}$ K_0=29$^{SEB\text{-}3P/CA}$	166.7 ^{CD} 78 ^{CA}	
	108 μm	0.2	3540	196	5.5	K_0=42$^{SEB\text{-}3P/CD}$ K_0=23$^{SEB\text{-}3P/CA}$	118.6 ^{CD} 65 ^{CA}	
	88 μm	0.14	3468	202	5.8	K_0=7$^{SEB\text{-}3P/CD}$ K_0=15$^{SEB\text{-}3P/CA}$	20.2 ^{CD} 43.3 ^{CA}	
$MoSi_2$ (5600^{i}, 420^{B}) matrix with ^{D}Nb (8570^{b}, 105^{A}) spheres	Nb dia.=250 μm	Nb: 0.20	6194	357	5.8	K_{IC}=5.2$^{DC(T)}$ 25×19×5 No toughening	8.4	[8]
^{D}Nb (8570^{b}, 105^{A}) particles reinforced $MoSi_2$ (5600^{i}, 420^{B})	Nb dia.: 200 μm	Nb: 0.2	6194	357	5.8	K_C=5.7$^{SEB/4P}$	9.2	[20]
^{D}Nb (8570^{b}, 105^{A}) fibers reinforced $MoSi_2$ (5600^{i}, 420^{B})	Nb dia.: 250 μm Nb dia.: 750 μm	Nb: 0.2 Nb: 0.2	6194	357	5.8	K_C=9.1$^{SEB/4P–CA}$ K_C=11.3$^{SEB/4P–CA}$	14.7 ^{CA} 18.2 ^{CA}	[20]

(*continued on next page*)

Table 1 (*continued*)

Material system (Density (Kg/m^3), Young's Modulus (GPa))	Characteristic dimensions	Volume fraction	Calc. density kg/m^3	Calc. modulus GPa	Specific modulus 10^7 m^2/s^2	Fracture toughness (MPa$\sqrt{m}$) and sample dimensions (mm)	Specific K (10^{-4} m$^2\sqrt{m}$/s^2)	Reference
Laminates of ^{D}Nb (8570^b, 105^A) & $MoSi_2$ (5600^i, 420^B)	Nb thickness: 200 μm	Nb: 0.2	6194	357	5.8	K_C=18$^{SEB/4P-CA}$	29.1 ^{CA}	[20]
Laminates of ^{D}Cu (8960^b, 130^A) and tape cast Al_2O_3 (3987^c, ~415^A)	Al_2O_3 thickness=75–560 μm, and Cu thickness=50–150 μm	Cu: 0.20–0.40	4982–5976	358–301	7.2–5	K_0=4–5^{4P-CD} 27×3×1.3–7.7, LSB K_0=8–10^{4P-CA} 27×1.3–7.7×3, LSB	6.7–10 ^{CD} 13.4–20.1 ^{CA}	[23]
Laminates of ^{D}Ni (8900^b, 200^A)and tape cast Al_2O_3 (3987^c, ~415^A)	Al_2O_3 thickness=75–560 μm and Ni thickness=50–150 μm	Ni: 0.20–0.40	4970–5952	372–329	7.5–5.5	K_0=4–5^{4P-CD} 27×3×1.3–7.7, LSB K_0=8–10^{4P-CA} 27×1.3–7.7×3, LSB	6.7–10.1 ^{CD} 13.4–20.1 ^{CA}	[23]
Al_2O_3 (matrix) (3987^c, 415^A) & ^{D}Al-4Mg "channels" (2660^d, 71^d)	Al–Mg dia.=20 μm	Al–Mg: 0.23	3682	336	9.1	K_0=3^{3P} L×3.7×3.1, LSB	8.2	[11]
Laminates of ^{D}Al (2700^b, 70^A) and tape cast Al_2O_3 (3987^c, ~415^A)	Al_2O_3 thickness=75–560 μm, and Al thickness=50–150 μm	Al: 0.20–0.40	3730–3472	346–277	9.3–8	K_0=4–5^{4P-CD} 27×3×1.3–7.7, LSB K_0=8–10^{4P-CA} 27×1.3–7.7×3, LSB	10.7–14.4 ^{CD} 21.5–28.8 ^{CA}	[23]

(*continued on next page*)

Table 1 (*continued*)

Material system (Density (Kg/m^3), Young's Modulus (GPa))	Characteristic dimensions	Volume fraction	Calc. density kg/m^3	Calc. modulus GPa	Specific modulus 10^7 m^2/s^2	Fracture toughness (MPa$\sqrt{m}$) and sample dimensions (mm)	Specific K (10^{-4} m$^2\sqrt{m}$/s^2)	Reference
Diffusion bonded laminates of ^{D}Cu (8960^{b}, 130^{A}) and Al_2O_3 (3987^{c}, 415^{A})	Cu thickness=25 & 130 μm Al_2O_3 thickness=480 μm	Cu: 0.05–0.21	4236–5031	401–355	9.5–7.1	K_0=5–12$^{4P\text{-}CA}$ 30×8×1 Possibly SSB	9.9–28.3 ^{CA}	[16]
Laminates of ^{D}Al (2700^{b}, 70^{A}) and Al_2O_3 (3987^{c}, ~415^{A})	Al_2O_3 thickness=1 mm Al thickness=50–100 μm	Al: 0.05–0.10	3923–3858	398–380	~10	K_0=10$^{3P\text{-}CA}$ 45×10×5, LSB	25.5–25.9 ^{CA}	[19]
Diffusion bonded laminates of ^{D}Al (2700^{b}, 70^{A}) and Al_2O_3 (3987^{c}, ~415^{A})	Al thickness=25–250 μm Al_2O_3 thickness=45–680 μm	Al: 0.035–0.85	3942–2893	403–122	10–4.2	K_0=5–17$^{4P\text{-}CA}$ 30×8×1 Possibly SSB	12.7–58.8 ^{CA}	[16]
Lithium aluminum silicate glass (2400-2800^{e}, 80^{A}) & SiC (Nicalon) fibers (2550^{f}, 470^{A})	SiC dia.=14 μm	SiC: 0.44	2466–2490	252	10–9.4	K_0=2^{4P} L×7.4×2.4, LSB	~8	[11]

3P: 3-point bending. Dimensions: L×W×B (see schematic below); 4P: 4-point bending. Dimensions: L×W×B (see schematic below); CA: crack-arrester configuration (also called "face-crack" configuration); CD: crack-divider configuration (also called "edge-crack" configuration); CT: compact tension (dimensions (ASTM E399-90): W×a×thickness); D: ductile phase; DC(T): disc-shaped compact-tension (diameter (∅)×width×thickness); K_C: fracture toughness; K_0: initiation fracture toughness; K_{IC}: plane strain fracture toughness; LSB: large scale bridging; SEB: single edge-notched bend specimen; SSB: small scale bridging.

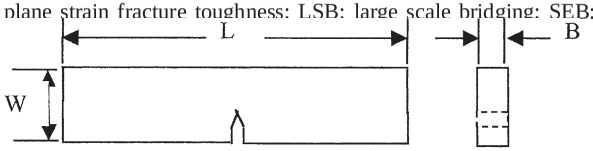

[a] [40], [b] [40], [c] [43], [d] [45], [e] [47], [f] [48], [g] [2], [h] [49], [i] [8], [j] [50], [k] [51], [l] MSDS, Alfa-Aesar, MA, USA, [m] [37], [n] [53], [o] [53], [A] [41], [B] [42], [C] [44], [D] [46], [E] [52].

shown subsequently, the Ti–Al_3Ti laminate system possesses a combination of high strength, toughness and stiffness at a lower density than monolithic titanium or other laminate systems. Further, since Al is relatively inexpensive compared to Ti, the Ti–Al_3Ti system is economically more attractive than monolithic titanium. Although Ti–Al_3Ti laminates have been fabricated earlier by several researchers [28–31], the present research, to the authors' knowledge, is the first to elucidate the fracture mechanisms in Ti–Al_3Ti composites, to determine their fracture toughness, and to fabricate them in a substantially large size for possible practical applications.

1.2. Crack growth and toughening mechanisms in laminate composites

Crack propagation in laminates can be studied in two extreme orientations, as shown schematically in Fig. 1. In the crack arrester orientation, the initial notch/crack tip ends within an individual layer of the test sample such that the crack front "sees" each layer interface sequentially during loading. In the crack divider orientation, the initial notch/crack tip intersects all the layers of the test sample such that the crack front "sees" all the layer interfaces simultaneously [32]. Toughening mechanisms in materials can be broadly divided into two categories—intrinsic and extrinsic. Intrinsic toughening implies toughening due to inherent resistance

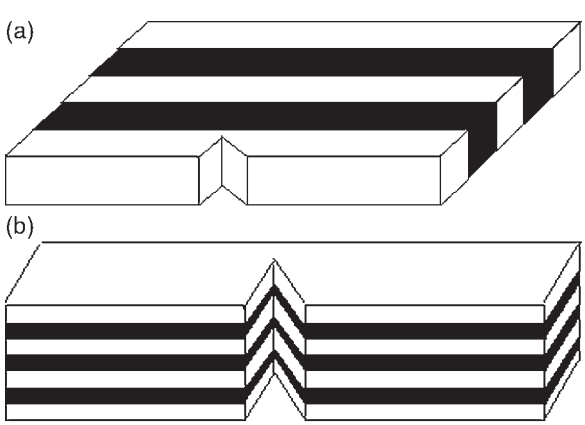

Fig. 1. Schematic representation of sample geometry to study crack propagation in the Ti–Al_3Ti laminates. (a) Crack arrester orientation, and (b) crack divider orientation.

of the microstructure to crack growth. Intrinsic toughening mechanisms include grain size effects, precipitates, particle spacing etc. Extrinsic toughening relies on mechanisms that reduce the local stress intensity at the crack tip, and hence the "driving force" for the crack growth. Toughening in the Ti–Al_3Ti laminate composites is of the extrinsic type and several extrinsic toughening mechanisms are briefly described below [33]:

1.2.1. Crack deflection

It occurs when layer delamination occurs ahead of an advancing crack or when a crack encounters an interface. Large crack deflection (up to 90° in the crack-arrester orientation) can reduce the Mode I component of the local stress intensity and causes the crack to move away from the planes of maximum stress. This mechanism is independent of the volume fraction of the metallic phase.

1.2.2. Crack blunting

It occurs when a crack encounters a ruptured region and is consequently, deflected and blunted. Further crack growth requires re-nucleation, i.e. a significant amount of energy absorption, resulting in an increase in toughness. This mechanism is independent of the volume fraction of the metallic phase.

1.2.3. Crack bridging

In this toughening mechanism, unbroken ductile layers span the wake of the crack and crack-growth requires stretching of the bridging ligaments which must have sufficient ductility to avoid fracture at or ahead of the crack tip. This mechanism can result in the typical resistance curve (R-curve) behavior and is dependent upon the volume fraction of the ductile phase.

1.2.4. Stress redistribution

Delaminations in the layers ahead of the crack-tip result in a reduction and redistribution of the local stress. This mechanism can result in R-curve behavior.

1.2.5. Crack front convolution

In a composite comprised of layers with dissimilar ductility and tested in the divider orientation,

the crack front in the less ductile component leads the crack in the more ductile component. The resulting crack front is highly convoluted and can result in delamination at the interfaces. Thus, crack growth is slowed and reduced by the plastic tearing required for crack propagation in the more ductile layer. This mechanism is dependent upon the volume fraction of the metallic phase and can result in the R-curve behavior.

1.2.6. Change in the local deformation mode

In a laminate tested in the divider orientation, substantial deformation at the crack-tip may change the deformation mode of individual layers from plane strain to plane stress. This change in the deformation mode causes the layers to fail in shear rather than flat fracture and, consequently, increases the stress required for crack growth. This toughening mechanism can result in the R-curve behavior.

1.3. Modeling toughness in laminate composites

Plastic deformation in ductile-brittle composites is accompanied by necking or bridging of the ductile phase (particles, layers, etc.) which requires a work-of-stretching and results in an increment, ΔG_C, in the energy required to fracture [6]. The bridging ductile phase can also be looked at as exerting a closing force on the crack face which reduces the stress intensity, K, at the crack tip such that the remote stress intensity required to propagate the crack becomes larger [11]. The bridging phenomenon can be divided into small-scale bridging (SSB) and large-scale bridging (LSB) depending upon whether the size of the bridging zone is small or comparable, respectively, to the crack length and in-plane specimen dimensions. The distinction between SSB and LSB is important as ΔG_C is independent of crack length and specimen geometry in the SSB but not in the LSB [34].

Under SSB conditions, the bridging behavior is modeled by relating the stress/crack opening relation, $\sigma(u)$, to the uniaxial plastic flow properties of the ductile phase [6]. Once $\sigma(u)$ is known, ΔG_C can be calculated as [6,9]:

$$\Delta G_C = f\int_0^{u^*} \sigma(u)\mathrm{d}u \tag{1}$$

where f is the area fraction of ductile material intercepted by the crack and $u*$ is the total crack opening when the material fails. The function $\sigma(u)$ is determined by the constraint in the matrix, constraint associated with debonding of the matrix, constitutive properties of the ductile phase, and large geometry changes due to processes such as the evolution of shear bands. Thus, while the ductile–brittle composite has an intrinsic fracture toughness, K_0 (also known as the matrix or crack-initiation toughness), crack bridging by the ductile phase increases the overall toughness by an amount, ΔK_C, to a steady-state toughness value, K_{SS}. The steady-state toughness can be modeled as [34]:

$$K_{SS} = \sqrt{K_0^2 + \Delta K_C^2}, \tag{2}$$

Since fracture toughness, K, is related to strain energy release rate, G, as follows [35]:

$$K = \sqrt{EG} \text{ (plane stress)}, \tag{3a}$$

$$K = \sqrt{\frac{EG}{(1-\nu^2)}} = \sqrt{E'G} \text{ (plane strain)}, \tag{3b}$$

where ν is the Poisson's ratio, equation (2) can be written as:

$$K_{SS} = \sqrt{K_0^2 + E'\Delta G_C}. \tag{4}$$

The steady-state magnitude of ΔG_C is given by [14]:

$$\Delta G_C = \sigma_0 \cdot f \cdot R \cdot \chi, \tag{5}$$

where σ_0 is the unconstrained uniaxial yield strength of the reinforcement, f is the area fraction of reinforcement, $2R$ is the reinforcement thickness, and χ is a work-of-rupture parameter that varies between 1.6 and 6, depending on the degree of interface debonding and the reinforcement constitutive behavior [9]. The product of σ_0 and χ can be replaced by the constrained yield stress of the ductile layers, σ_C.

The objectives of this research were to determine the R-curve and fracture behavior of Ti–Al_3Ti MIL composites in the crack arrester and crack divider orientations as a function of the volume fraction of the ductile (Ti) phase. The volume

fractions of Ti in the Ti–Al_3Ti composites tested were 14, 20 and 35 percent.

2. Experimental procedures

2.1. Processing

Foils of commercial purity 1100 aluminum and Ti–3Al–2.5V were stacked alternately and placed between two nickel alloy platens on the crosshead of a screw-driven load frame. A detailed description of the processing method for synthesis of these MIL composites has been presented elsewhere [1]. Each platen was heated by a set of 5 cartridge heaters and the temperature of the platens was controlled via programs written in LabView software. Table 2 lists representative starting foil thickness and the final metal (Ti) and intermetallic (Al_3Ti) thickness. The thickness of the starting Ti and Al foils was selected to ensure that the Al was completely consumed by the adjacent Ti layers to produce Al_3Ti, leaving behind some unreacted Ti. The volume fraction of the residual Ti (or Al_3Ti) was thus, controlled by the thickness of the starting layers. In subsequent sections, the samples will be identified by the volume fraction of titanium. For example, a 14Ti indicates a sample with a Ti volume fraction of 14%. Typical plate dimensions of the starting MIL composites were ~150 mm square and ~20 mm thick.

2.2. Compression testing (end-confined quasi-static)

Rectangular compression samples, 6 mm×6 mm×10.5 mm tall, were cut from the MIL composite plates and ground to 4000 grit. Several steel rings were machined with 19.1 mm diameter, 2 mm thickness and a 6 mm square cutout in the center. The square ends of the compression samples were then placed within the square cutout of a ring at each end to provide end-confinement and eliminate end and edge premature failure effects. The samples were tested in compression at room temperature at strain rates of 10^{-4}/s and 10^{-2}/s in a servo-hydraulic test frame. Grease was used between the platens and sample ends to minimize friction. Tensile samples were machined out of Ti foils and tested at a strain rate of 10^{-3}/s. Load data from the load cell and displacement data from the deflectometer were recorded by the data acquisition program and used to plot the corresponding engineering stress–strain curves. The tensile data was used to obtain unconstrained yield strength of the Ti foils for use in the toughness modeling.

2.3. Three point bend testing

Resistance-curve (or R-curve) testing of the MIL composites in the crack-arrester and crack-divider orientation was performed on single edge-notched bend (SE(B)) specimens in accordance with ASTM E-399–90. The typical width, *W*, of a bend sample was 17 mm with a thickness, *B*, of 8.5 mm and a span of 72 mm (4.2*W*). The samples were notched using a low speed saw with a 0.25 mm thick diamond blade. Fatigue pre-cracking was performed on a servo-hydraulic load frame by cycling the load between 0 and 150 N. This notching and pre-cracking procedure was required to simulate a natural crack by using a reproducibly sharp and narrow machined notch in order to start, measure, and maintain the stress-state of the crack at the midpo-

Table 2
Representative metallic–intermetallic laminate composite materials

Sample	Nominal starting foil thickness (μm)		Nominal final layer thickness (μm)		Nominal volume fractions	
	Ti	Al	Residual Ti	Al_3Ti	Ti	Al_3Ti
35Ti	250	200	160	300	0.35	0.65
20Ti	250	300	110	440	0.20	0.80
14Ti	250	380	90	540	0.14	0.86

int of the sample. The combined notch and pre-crack length varied between 0.45–0.55 *W*. A Navitar Zoom 6000 internal co-axial and fiber-optic ring light illuminated zoom lens system (22.69–3.56 mm diagonal field of view) was connected to a CCD camera to capture and record video of the bend tests. The bending was preformed in a servo–hydraulic test frame under displacement control at a rate of 0.5 mm/min, with load cell, deflectometer and time data recorded by the data acquisition program. Crack length at different times was measured by analyzing the video images of the test. At least two samples for each Ti volume fraction, and orientation were used to collect data.

Fracture toughness was calculated as follows, in accordance with the ASTM standard E399-90:

$$K = (PS/BW(3/2) \times f(a/W), \tag{6}$$

where K is the fracture toughness, P is the load, S is the span, B is the specimen thickness, W is the specimen width (depth), a is the crack length, and $f(a/W)$ is the function defined as:

$$f(a/W) = \frac{3(a/W)^{1/2}[1.99-(a/W)(1-a/W) \times (2.15-3.93a/W + 2.7a^2/W^2)]}{2(1 + 2a/W)(1-a/W)^{3/2}} \tag{7}$$

.The function $f(a/W)$ was calculated using a Microsoft Excel spreadsheet for each measured crack length and the R-curves were then plotted from the calculated K values and the measured crack lengths.

2.4. Elastic modulus of MIL composites

The elastic modulus of the MIL composites was calculated from their ultrasonic sound speed and density. The longitudinal sound velocity in the sample was measured in the transmission mode using a pair of 5 MHz, 6.35 mm diameter, broad band Panametrics transducers. The sample surfaces were polished to better than 3 μm and the transducers were held to the sample by hand, with water as a couplant between the transducers and sample. The density of the samples was measured using the buoyancy method.

3. Results and discussion

3.1. Compression testing (end-confined quasi-static)

The typical microstructures of the MIL composites are shown in Fig. 2. The volume fraction of Ti was calculated as:

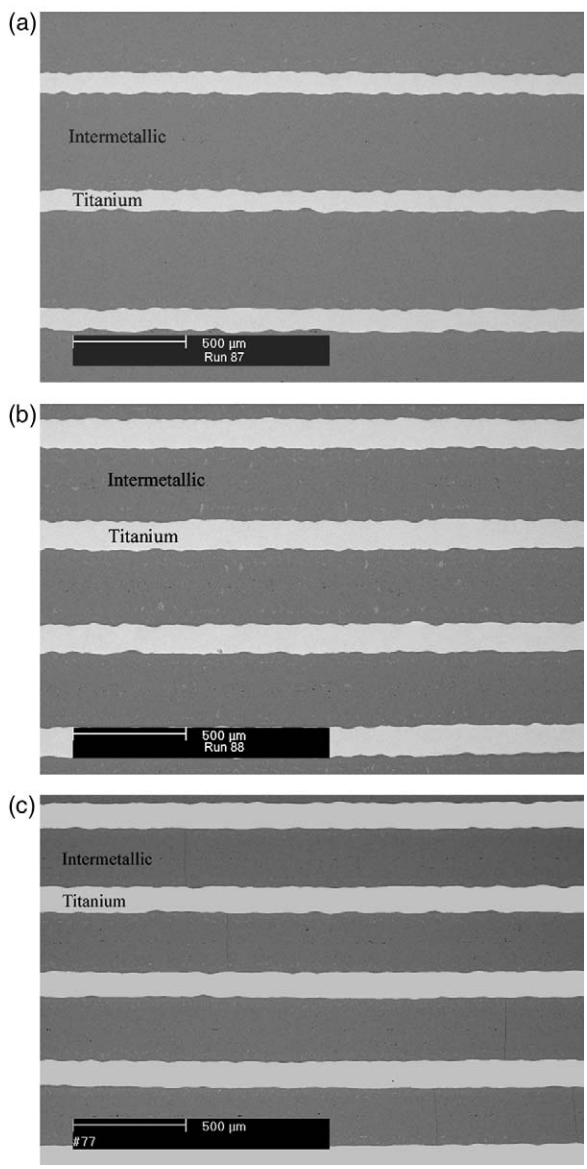

Fig. 2. Representative backscattered SEM micrographs of the through-thickness section of the laminates tested. (a) 14% Ti (b) 20% Ti, and (c) 35% Ti.

$$\frac{t_{Ti}}{t_{Ti} + t_{Al_3Ti}}, \quad (8)$$

where t_{Ti} and t_{Al3Ti} refer to the thickness of the Ti and the Al_3Ti layer, respectively.

The end-confined quasi-static stress–strain curves for the 14Ti composite are shown in Fig. 3. The yield stress for samples tested with the layers parallel and perpendicular to the load is 1020 MPa and 870 MPa, respectively, with only a few percent ductility. Figure 4 shows typical fractured samples of the 14Ti composites tested at a strain rate of 0.0001/s. When the samples were tested with the layers parallel to the load, Fig. 4(a) shows that the fracture occurs by a combination of shattering of the intermetallic, buckling of the Ti layers, and shearing of Ti and Al_3Ti layers. When the composites were tested with the layers perpendicular to the load, failure occurred by shearing through the thickness of the sample and takes on the form of steps through the layers.

The end-confined quasi-static stress–strain curves for the 20Ti composite are shown in Fig. 5. The yield stress for samples tested with the layers parallel and perpendicular to the load is 1150 MPa and 900 MPa, respectively, and these strength values are 13% and 3%, respectively, higher than those obtained in the 14Ti samples. Figure 6 shows typical fractured samples of the 20Ti composites with the failure mode being similar to that obtained in the 14Ti composites for the respective loading directions.

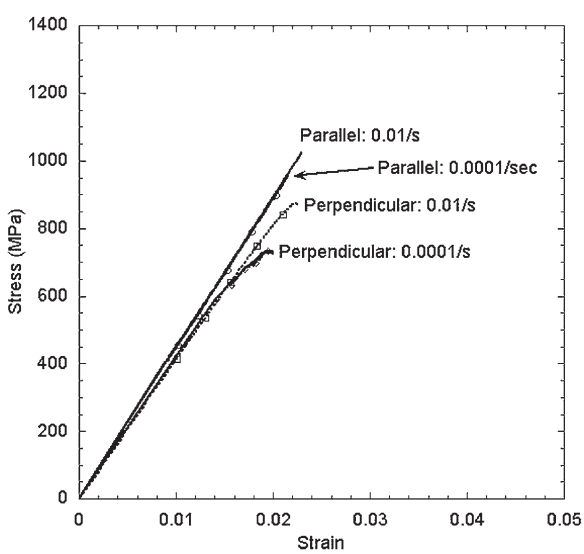

Fig. 3. 14Ti end-confined quasi-static stress–strain curves for samples tested at 0.01/s and 0.0001/s with layers parallel and perpendicular to the load.

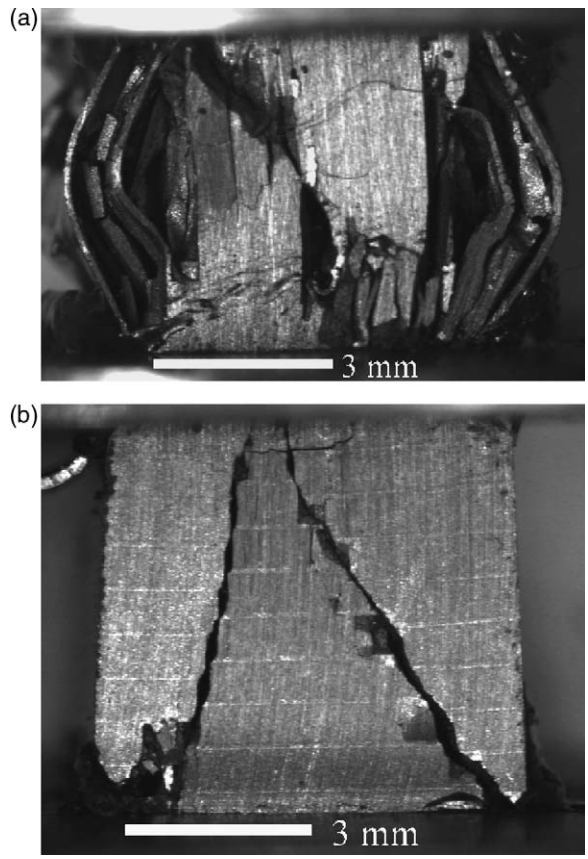

Fig. 4. Failure modes in 14Ti end-confined quasi-static compression samples. (a) Layers parallel to load, 0.0001/s. (b) Layers perpendicular to load, 0.0001/s.

The end-confined quasi-static stress–strain curves for the 35Ti composite are shown in Fig. 7. The yield stress for samples tested with the layers parallel and perpendicular to the load is 1270 MPa and 910 MPa, respectively, and these strength values are respectively ~25% and ~5% higher than those obtained in the 14Ti samples. Figure 8 shows typical fractured samples of the 35Ti composites and that the damage is confined to the sample volume between the confinement rings.

The end-confined quasi-static flow curves in

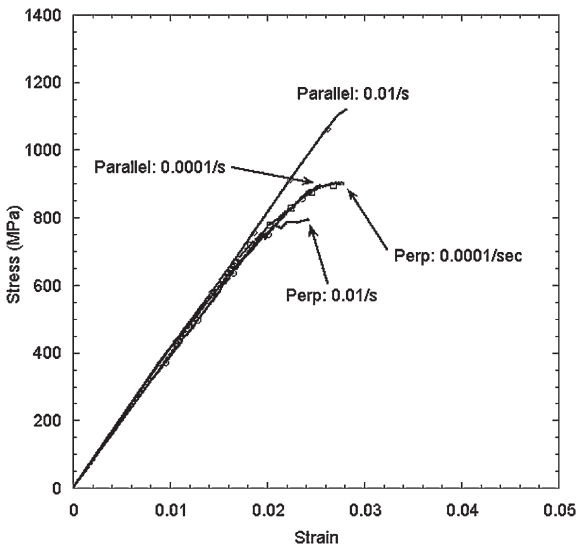

Fig. 5. 20Ti end-confined quasi-static stress–strain curves for samples tested at 0.01/s and 0.0001/s with layers parallel and perpendicular to the load.

Figs 3, 5 and 7 for the MIL composites of varying metal-intermetallic volume fraction show that the yield strength of the MIL composites increases with increasing metal (Ti) volume fraction. The flow curves also show that the yield strength for all the compositions was greater when the sample layers were parallel to the loading direction. The composites show minimal plasticity with failure strains of 0.02–0.03, with the 35Ti showing a slightly larger failure strain. Figures 4, 6 and 8 show that the damage and failure mechanisms are similar for all the compositions tested for respective loading direction. When loaded parallel to the layers, the load carried by each phase is distributed in proportion to their modulus ratio. Al_3Ti being the stiffer of the two phases, thus carries a proportionately greater load until failure. Subsequent to the failure of the Al_3Ti, the Ti layers fail by bending and buckling. When loaded perpendicular to the layers, the intermetallic fails by "axial splitting" owing to the in-plane tensile stresses, a phenomenon also commonly seen in brittle ceramics when loaded in compression. The fracture of the intermetallic causes the adjacent Ti layers to be unsupported and the ductile Ti layers fail by shear due to the shear displacements that can now

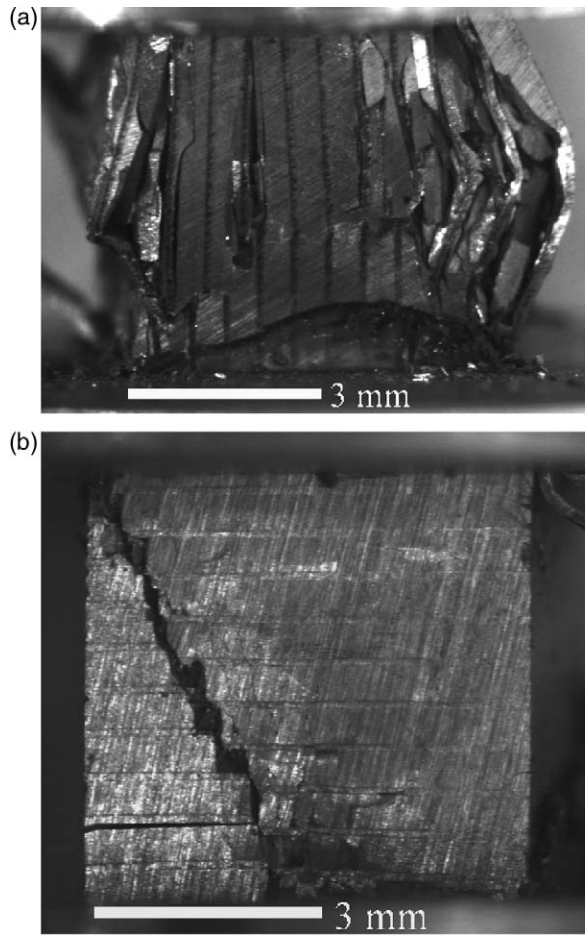

Fig. 6. Failure modes in 20Ti end-confined quasi-static compression samples. (a) Layers parallel to the load, 0.01/s. (b) Layers perpendicular to the load, 0.0001/s.

occur at the locations of the axial splitting. Hence, while the sample is globally loaded in compression, the brittle intermetallic fails by in-plane tensile stresses and the ductile Ti layers fail by shear. The axial splitting of the intermetallic alternated by sheared Ti layers give a step-like appearance to the fractured surface, as seen in Figs 4, 6 and 8.

Figure 9 shows the specific compressive strength (i.e. compressive strength divided by density) as a function of specific Young's modulus (i.e. Young's modulus divided by the density) for Ti–Al_3Ti composites and a variety of engineering materials. For structural applications, one would typically prefer a

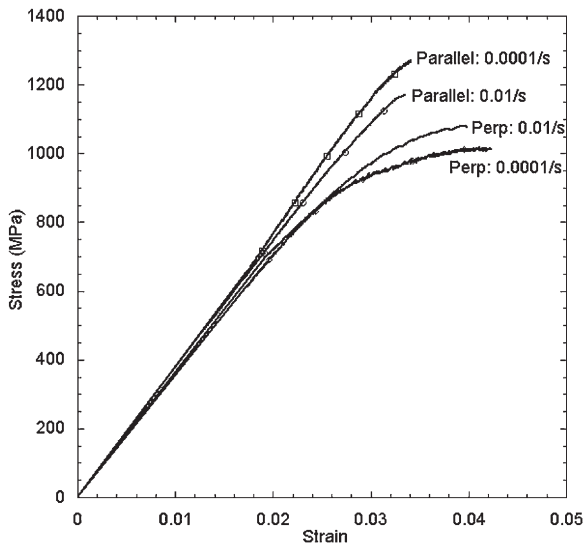

Fig. 7. 35Ti end-confined quasi-static stress–strain curves for samples tested at 0.01/s and 0.0001/s with layers parallel and perpendicular to the load.

material in the top-right corner (i.e. highest specific strength and specific modulus), as seen in diamond and diamond/carbide laminates. However, the high cost of diamond and the difficulty of obtaining it in bulk form preclude these two materials from typical structural applications. It is seen that the Ti–Al_3Ti laminates outperform conventional metals (indicated by nickel, stainless steel and other dark colored ellipses close to them), whereas ceramics, such as boron carbide, perform better than the MIL composites or the conventional metals. Although the monolithic ceramics appear better than the MIL composites with regard to specific strength and stiffness, it will be shown subsequently that the MIL composites have a much higher fracture toughness than monolithic ceramics making the MIL composites a better choice. Thus, Fig. 9 shows that the MIL composites are extremely promising materials for structural applications that require high compressive strength and high stiffness.

3.2. Resistance-curves in the arrester orientation

Of the three MIL compositions tested in the arrester orientation, a single main crack could not

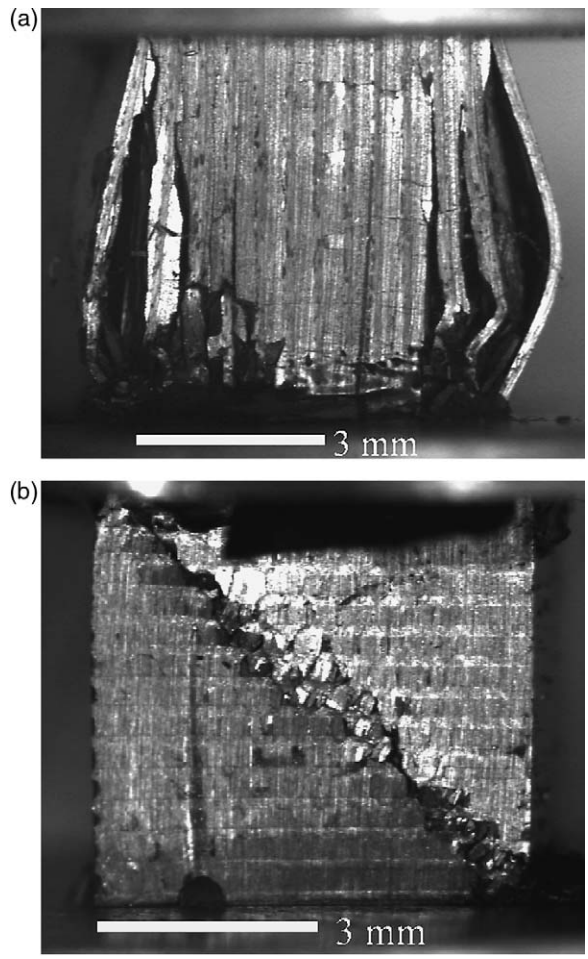

Fig. 8. Failure modes in 35Ti end-confined quasi-static compression samples. (a) Layers parallel to the load, 0.01/s. (b) Layers perpendicular to the load, 0.01/s. The defocused band at the top and the bottom of the images is the confinement ring.

be grown parallel to the initial notch direction in the two "metal-rich" 20Ti and 35Ti composites. Instead, the main crack originating from the notch grew perpendicular to the initial notch direction in the intermetallic layers near the notch, as shown in the optical photographs in Fig. 10. Crack growth parallel to the initial notch direction could only be achieved in the 14Ti samples, i.e. the composite with the minimum metal (or "maximum brittle intermetallic") content. Consequently, the typical R-curve behavior could only be obtained for the 14Ti composite, as shown in Fig. 11. The concave-up shape of the R-curve, i.e. increasing resistance

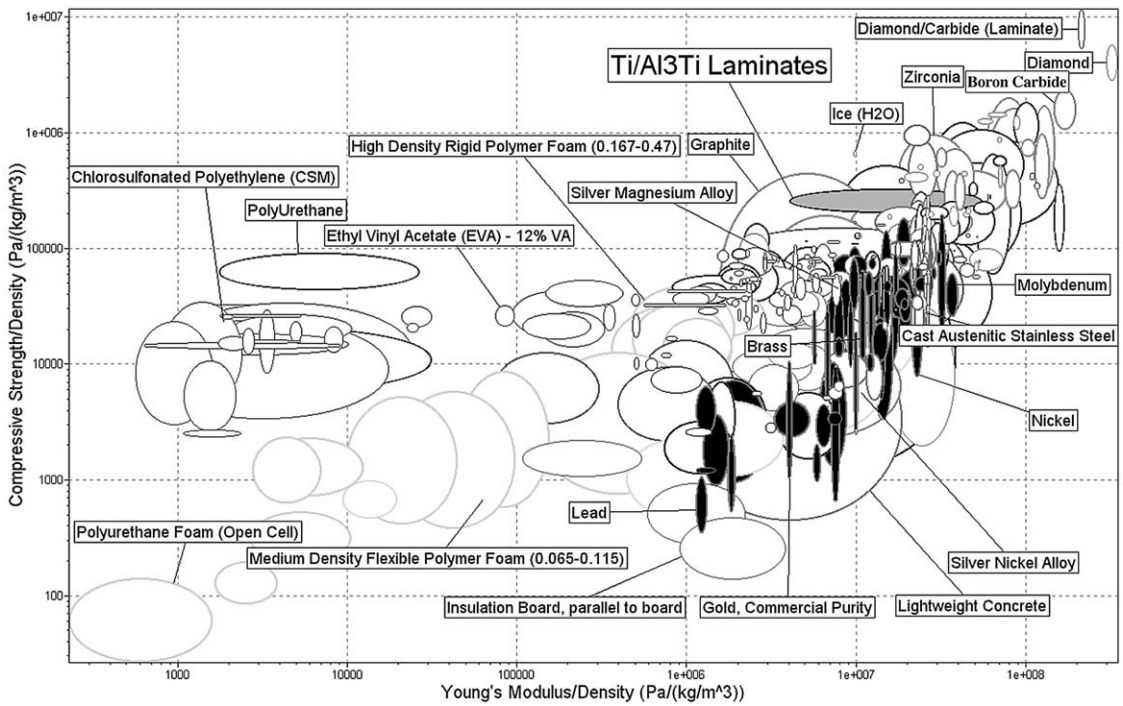

Fig. 9. Plot of specific compressive strength vs. specific modulus of Ti–Al_3Ti laminates relative to other engineering materials. The metals and alloys are indicated by dark filled ellipses while the MIL composites are indicated by the gray colored ellipse. Data plotted using Cambridge Engineering Selector V3.1 software.

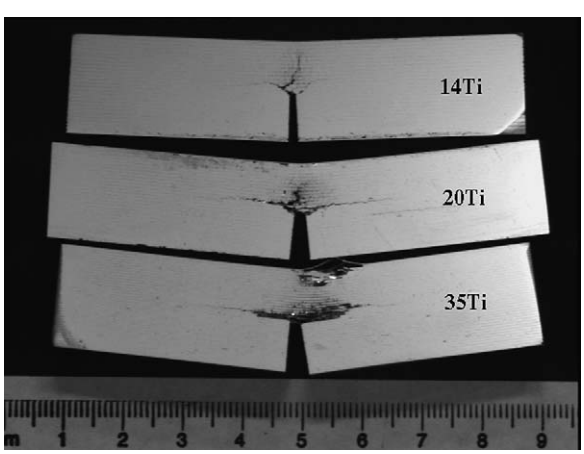

Fig. 10. Arrester orientation R-curve specimens after testing showing that a single main crack could not be grown in the initial notch direction in the 20Ti and 35Ti composites.

to crack-growth with increasing crack-length, for the 14Ti composite indicates the occurrence of large-scale bridging (LSB) and hence, the R-curve data for this composite is geometry dependent [34]. In spite of the lack of R-curve data for the 20Ti and 35Ti composites and the geometry dependent R-curve for the 14Ti composite, the initiation toughness (K_0) values from the plot in Fig. 11 provides a useful indicator of the relative fracture toughness of the composites tested. Thus, the arrester orientation initiation toughness values for the 14Ti, 20Ti, and 35Ti specimens are 15 MPa√m, 23 MPa√m, and 29 MPa√m, respectively.

Figure 12 shows SEM micrographs of samples tested in the arrester orientation. The micrograph for the 14Ti sample in Fig. 12(a) shows that there is one main crack and two smaller cracks, respectively, parallel and perpendicular to the initial notch direction. The micrograph for the 20Ti sample in Fig. 12(b) shows that the cracks propagated perpendicular to the initial notch direction along the

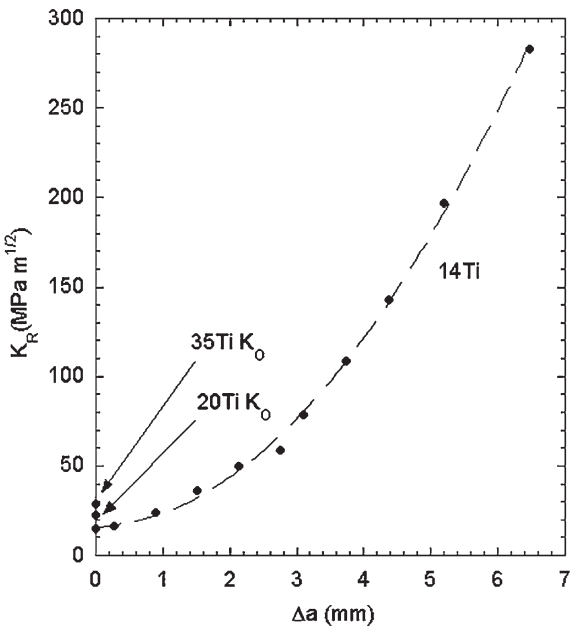

Fig. 11. R-curve for the 14Ti laminate and initiation toughness for the 20Ti and 35Ti laminates tested in the arrester orientation.

Al_3Ti layers located above the notch, accompanied by fragmentation and consequent loss of the intermetallic. The micrograph for the 35Ti sample in Fig. 12(c) shows that the cracks propagated perpendicular to the initial notch direction in the two intermetallic layers directly above the notch, in a manner similar to that in the 20Ti sample shown in Fig. 12(b). Bending of the 35Ti sample was accompanied by severe cracking and fragmentation of the intermetallic above the notch, and the sample eventually buckled. The micrographs of all the MIL composites in Fig. 12 show an extensive network of smaller cracks that form before and during the propagation of the main crack. Based on the occurrence of smaller cracks in almost all intermetallic layers above the notch, the bridging zones for all three arrester orientation tests are estimated to be greater than 6 mm. Bridging zones based on the main cracks originating at the notch are estimated to be more than 3 mm. While delamination or debonding of layers has been shown in the literature to be detrimental to the performance of laminate composites [22], these failure mechanisms were not observed in any of the samples tested.

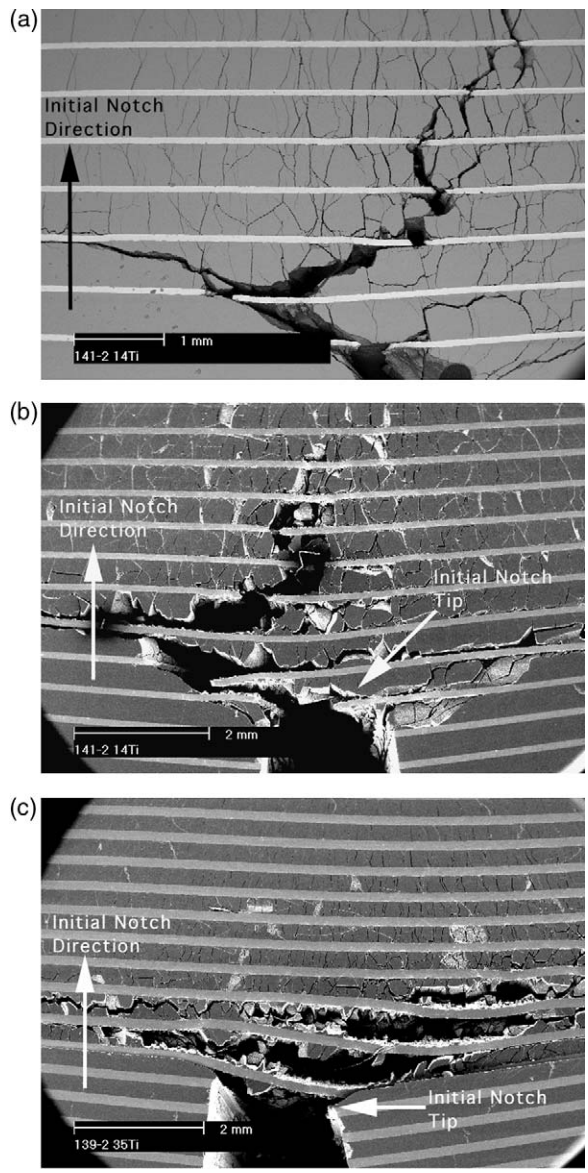

Fig. 12. SEM micrographs showing the damage in the specimens tested in the arrester orientation. (a) 14Ti, (b) 20Ti, (c) 35Ti.

The absence of delamination of the Ti and Al_3Ti layers during bend testing is an indication of the excellent bonding between the layers even though the fabrication process was performed in open air.

The SEM micrographs in Fig. 13 show the microstructural details of crack-growth and failure in a 14Ti sample tested in the arrester orientation.

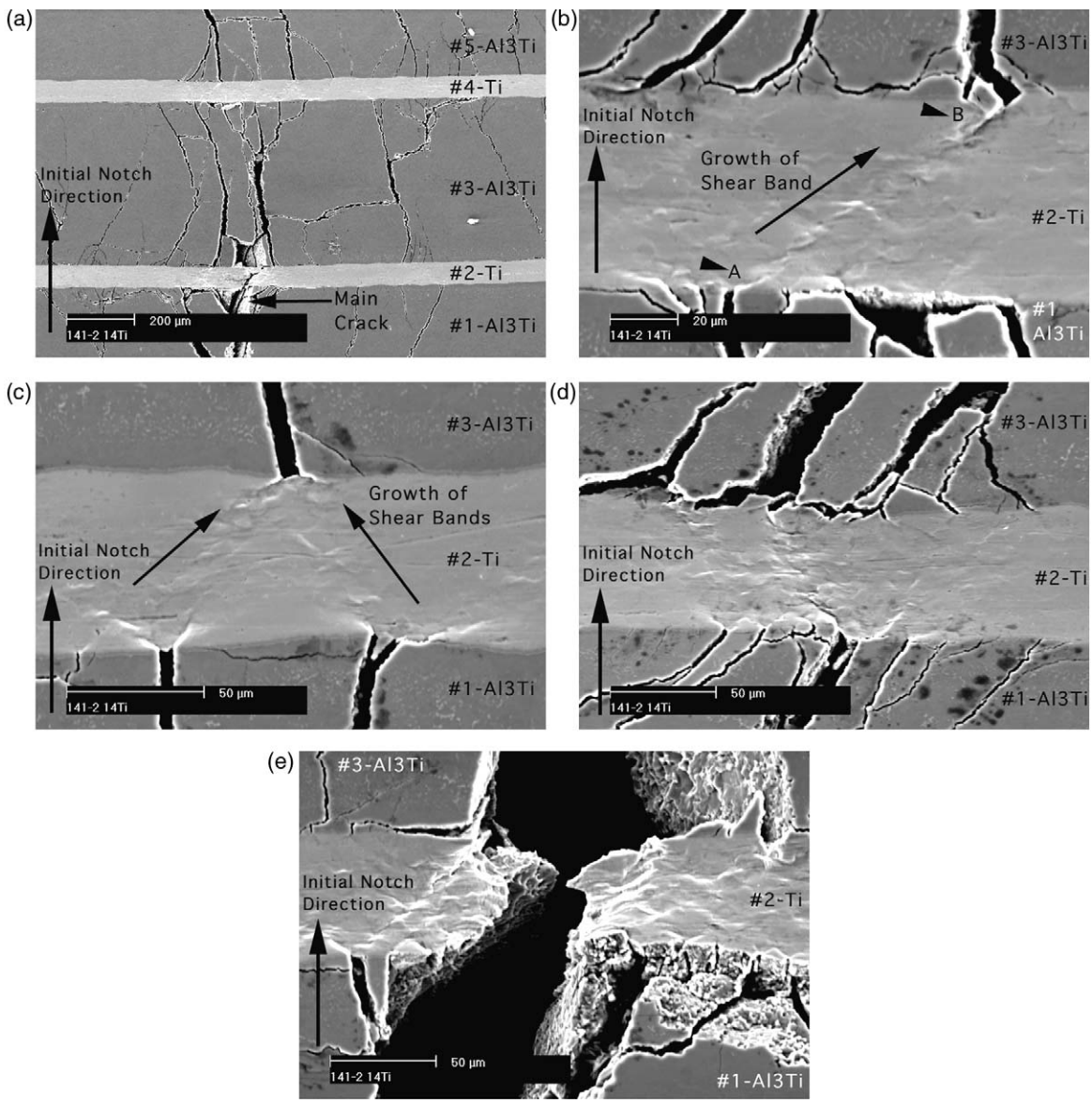

Fig. 13. Microstructural features of the 14Ti specimen tested in the arrester orientation. (a) Transition from fractured to bridging Ti; (b) single shear band connecting cracks in Al_3Ti; (c) two cracks and shear bands forming one crack in Al_3Ti; (d) Ti layer starting to fail; (e) fractured Ti layer with microvoid coalescence and plastic deformation (stretching and necking).

In the description that follows, the Ti and Al_3Ti layers are assigned numbers (e.g. Al_3Ti layer (#1) etc.). These layer numbers do not imply the location of that particular layer relative to the notch tip etc., but are solely a means to point out the location of microstructural features (in the SEM images) that are being described in the text below.

Figure 13(a) shows the main crack in the Al_3Ti layer (#1) that grows by the fracture of the adjacent Ti layer (#2). The main crack then branches into several smaller cracks in the Al_3Ti layers (#3 and #5). These smaller cracks in Al_3Ti layers (#3 and #5) are bridged by the Ti layer (#4) located at the top of the main crack. It is the bridging of the duc-

tile Ti layers before fracture, as shown by the Ti layer (#4), that causes the R-curve behavior shown in Fig. 11. Figure 13(b) shows a crack in the Al_3Ti layer (#1) that has nucleated a single shear band in the Ti layer (#2) at position A. This shear band runs across the Ti layer (#2) at an angle to the crack that initiated it, and then serves as a nucleation site (B) for crack growth in the next Al_3Ti layer (#3). Figure 13(c) shows two cracks in the Al_3Ti layer (#1) that form a shear band each in the adjacent Ti layer (#2). The two shear bands run across the Ti layer (#2) and converge on the opposite side of the Ti (#2) and result in the nucleation of a single crack in the adjacent Al_3Ti layer (#3). Figure 13(b) and (c) show the offset in the cracking due to the renucleation event at the opposite end of the angled shear band. Such offset in cracking enhances the bridging effectiveness and increases the energy necessary to fracture the Ti at an angle [4]. Figure 13(d) illustrates the start of fracture at the lower surface of a Ti layer leading to its fracture (Fig. 13(e)) by microvoid coalescence, plastic stretching and necking. Figure 13(e) also shows complete failure of the two Al_3Ti layers adjoining the fractured Ti layer. Failure of the Al_3Ti layers removes the constraint on the intermediate Ti layer and thus enables the extensive plastic deformation of the latter [9]. Plastic deformation of such unconstrained Ti layers, as shown in the micrograph in Fig. 13(e), results in significant plastic energy dissipation resulting in a high value of the initiation fracture toughness.

The SEM micrographs in Fig. 14 show the microstructural details of crack-growth and failure in a 20Ti sample tested in the arrester orientation. Figure 14(a) shows that unlike the 14Ti sample, the main crack in the 20Ti sample propagated perpendicular to the initial notch direction in the intermetallic layer. Figure 14(b) and (c) show extensive cracking and fragmentation in the Al_3Ti layers with the bridging Ti layers between the fragmented Al_3Ti layers.

The SEM micrographs in Fig. 15 show the microstructural details of crack-growth and failure in a 35Ti sample tested in the arrester orientation. In a manner similar to the 20Ti sample in Fig. 14(a), Fig. 15(a) shows a branch of the main crack propagating perpendicular to the initial notch direction and within the intermetallic layer, to the left of the notch (See also Fig. 10). Figure 15(b) and (c) show the complete fragmentation of the brittle Al_3Ti layers, while the adjoining ductile Ti layers remain intact, though bent, being no longer

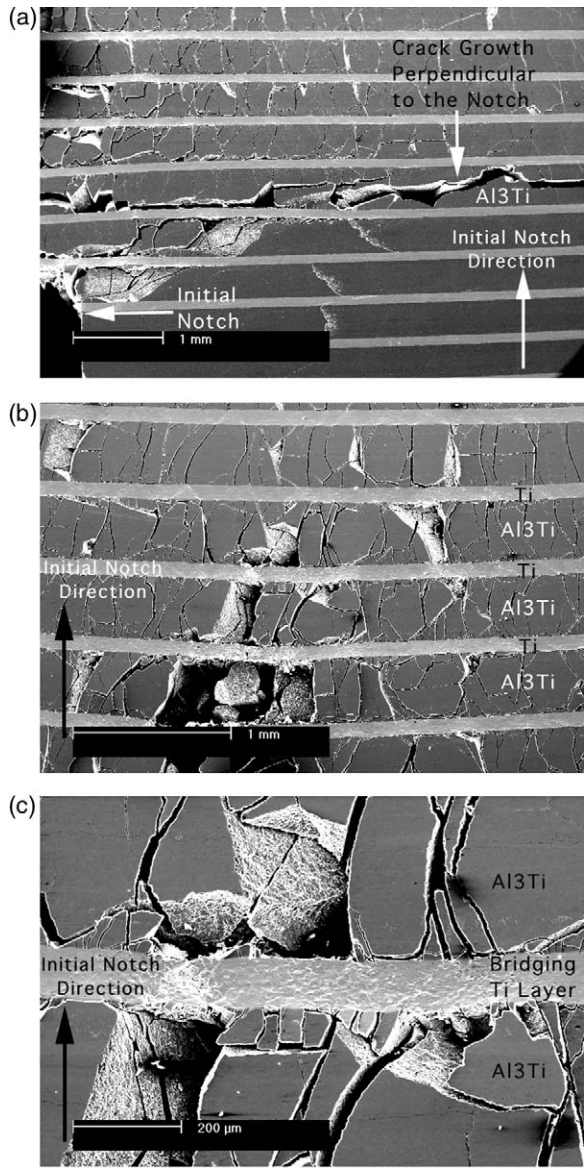

Fig. 14. Microstructural features of the 20Ti sample tested in the arrester orientation. (a) Details of the main crack in the Al_3Ti to the right of the notch (Fig. 8), (b) bridging by Ti layers above the notch, and (c) shear bands in Ti and cracking and fragmentation of Al_3Ti.

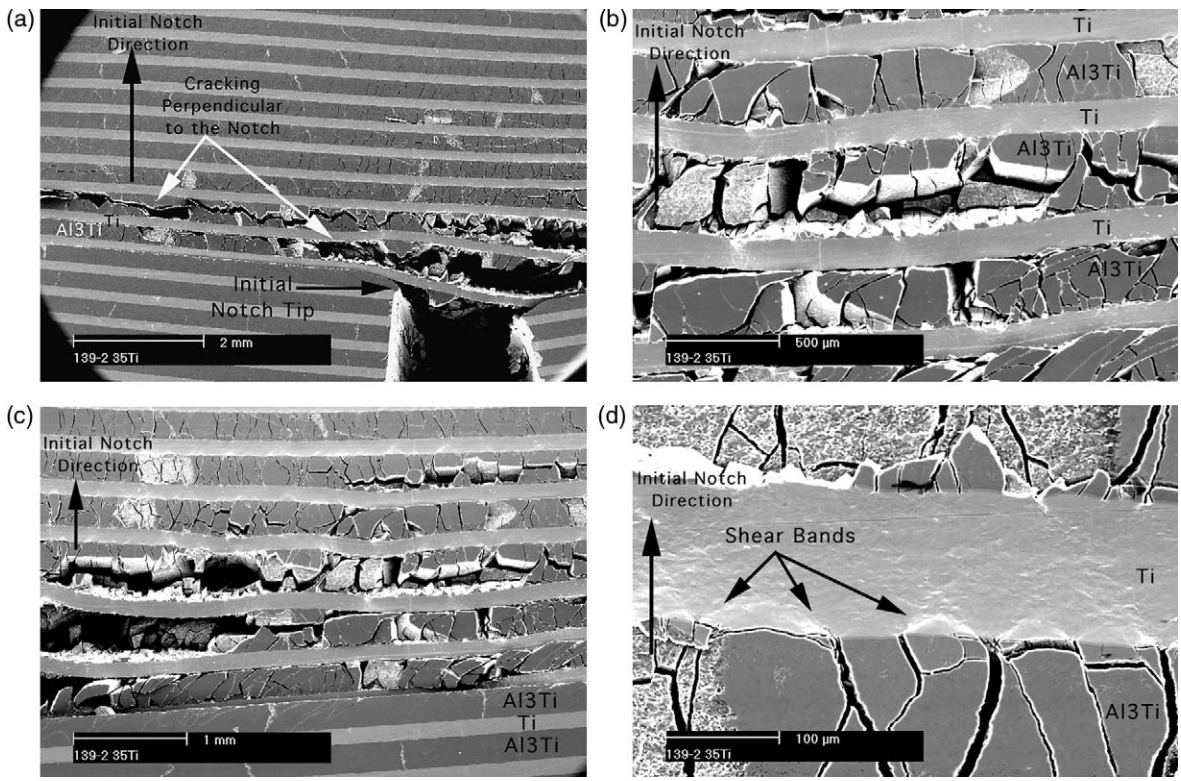

Fig. 15. Microstructural features of the 35Ti sample tested in the arrester orientation. (a) Details of the main crack in the Al_3Ti to the left of the notch (Fig. 8); (b) and (c) bending of the Ti layers and cracking and fragmentation of the Al_3Ti; (d) shear bands developing in the Ti.

constrained by the adjoining fragmented Al_3Ti layers. Figure 15(d) shows extensive shear banding with the shear bands nucleating at the crack tips.

As Fig. 11 shows, the 20Ti and 35Ti samples did not show the R-curve behavior in the arrester orientation since a single crack could not be grown along the initial notch direction. The geometry of the 20Ti and 35Ti samples was varied in terms of the sample size and the initial crack length in an effort to force the crack-growth along the initial notch direction and obtain the R-curve behavior. However, the crack-growth always occurred perpendicular to the initial notch direction. This inability to grow a single crack along the initial notch direction in the arrester orientation for 20Ti and 35Ti samples is an indication of the high toughness of the MIL composites. While toughening due to the laminate geometry is known in the literature (Table 1), the Ti–Al_3Ti laminate system is unique owing to its simplicity of fabrication and to the lower net density relative to other metal/metal–aluminide systems.

3.3. Resistance-curves in the divider orientation

Unlike the arrester orientation, R-curves could be obtained for all the samples tested in the divider orientation and are plotted in Fig. 16. The initiation toughness was found to increase with increasing Ti volume fraction in the MIL composites and was 7, 42, and 62 MPa√m for 14Ti, 20Ti, 35Ti samples, respectively. Figure 16 shows that the R-curves for the 20Ti and 35Ti samples reach a steady state toughness value of ~80 and ~115 MPa√m, respectively, while the R-curve for the 14Ti sample continues to increase. This apparent increase in toughness with increasing crack length in the 14Ti samples is attributed to the crack redirection and a

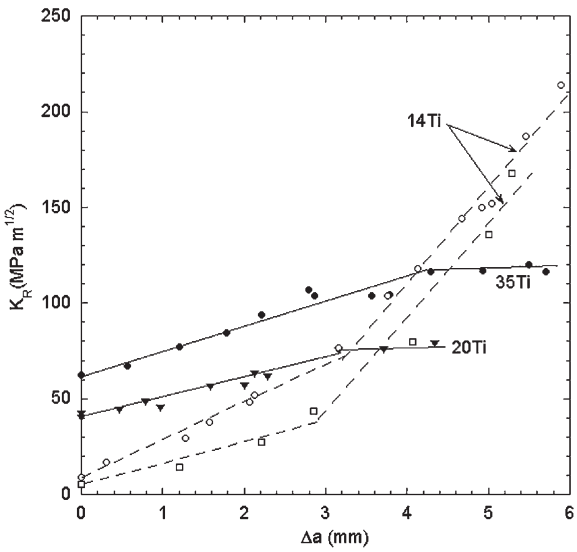

Fig. 16. R-curves for the 14Ti, 20Ti and 35Ti composites tested in the divider orientation.

small degree of secondary cracking along the initial notch direction as shown in Fig. 17(a). Figure 17(b) and (c) show that the incidence of secondary cracking along the initial notch direction increases with increasing Ti content of the composite. SEM micrographs of the fracture surfaces of the samples tested in the divider orientation are shown in Fig. 18. The micrographs in Fig. 18 show the similarity of the fracture mechanism, irrespective of the testing orientation, in the compositions tested. The failure of Ti layers occurred by microvoid coalescence, while the Al_3Ti layers exhibit flat brittle fracture. The micrographs also show that the incidence of intermetallic cracking and damage increases with increasing Ti volume fraction.

3.4. Toughness calculation

Although large-scale bridging (LSB) conditions apply to the samples tested here, the steady-state toughness (K_{SS}) under small-scale bridging (SSB) can be estimated using the energy method [9]. Using the relation (4):

$$K_{SS} = \sqrt{K_0^2 + Efr\sigma_C}.$$

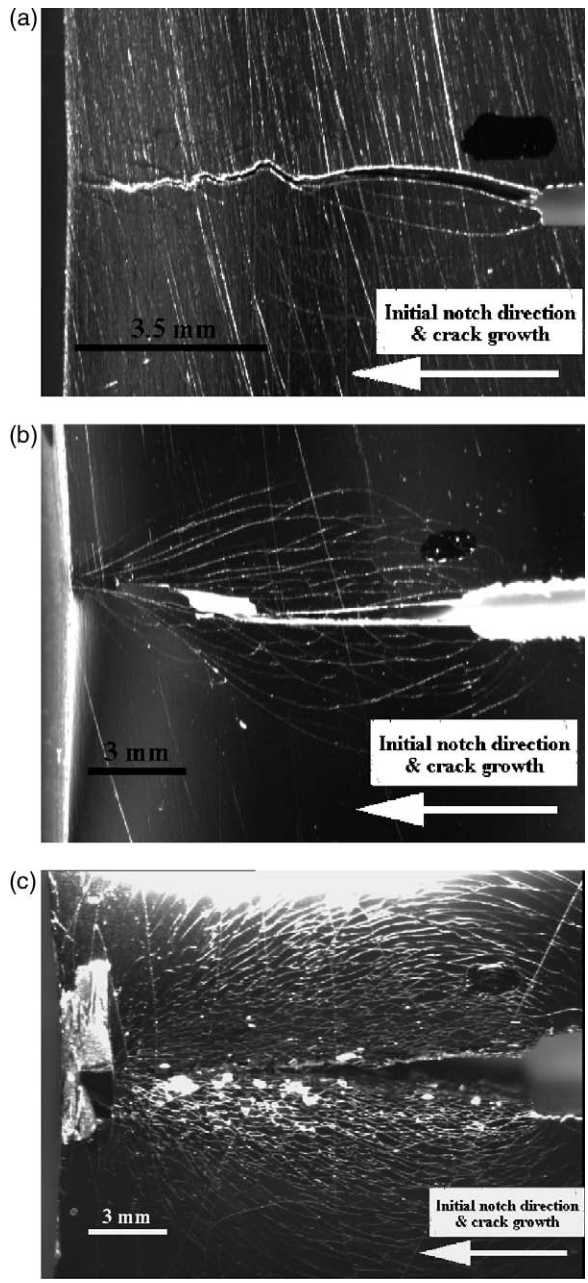

Fig. 17. Cracking in the specimens tested in the divider orientation. (a) 14Ti, (b) 20Ti, and (c) 35Ti. The initial notch and the crack growth directions are along the horizontal axis, as shown on the images.

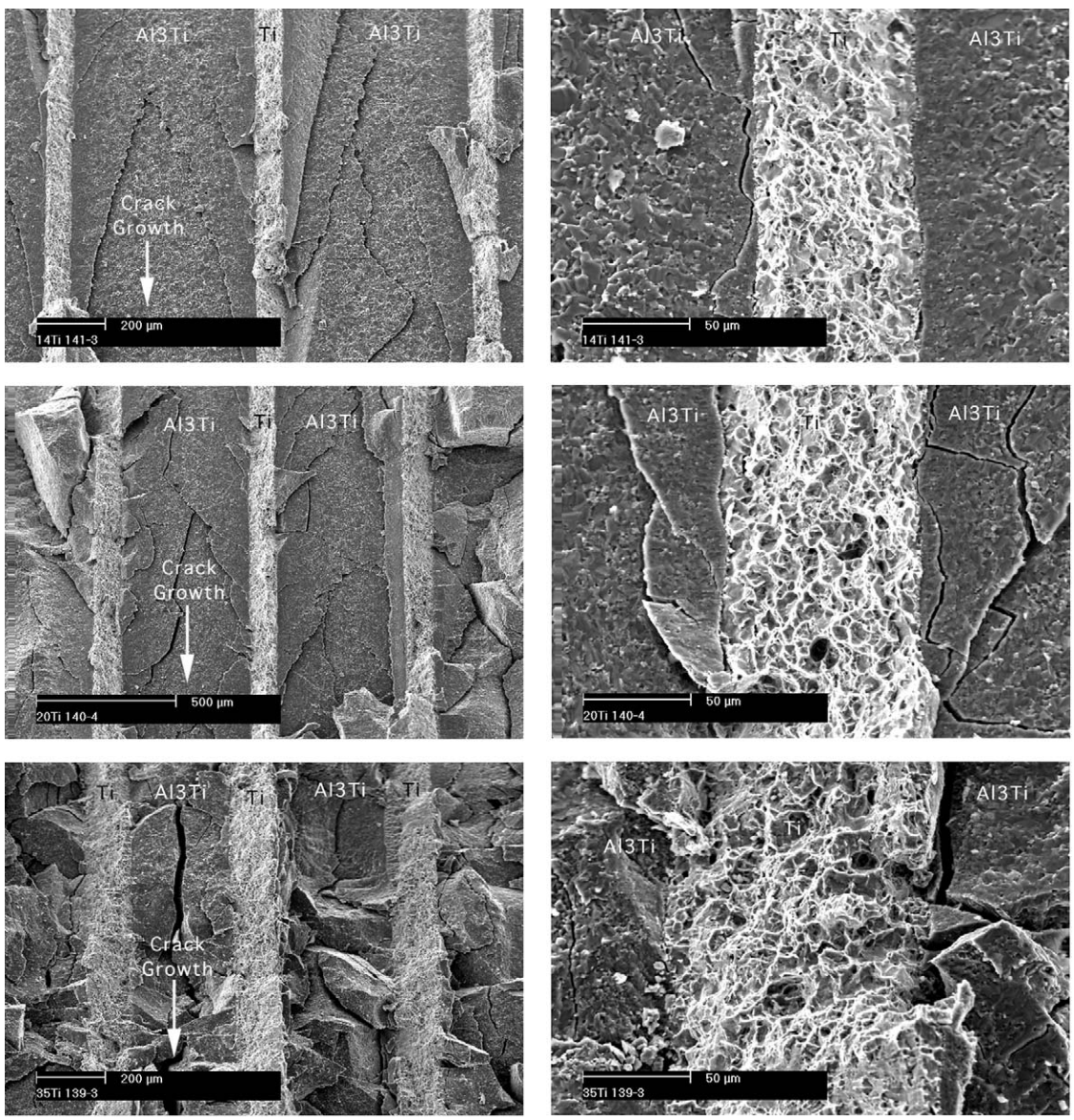

Fig. 18. Crack surface micrographs of divider orientation R-curve specimens: (a and b) 14Ti at low and high magnification, (c and d) 20Ti at low and high magnification, (e and f) 35Ti at low and high magnification. Crack growth direction is top to bottom in all the micrographs.

The initiation toughness, K_0, is obtained from the bending experiments and the modulus, E, was determined from ultrasonic measurements. Preliminary results [36] show that σ_C, the quasi-static yield stress of Ti constrained between the brittle intermetallic layers, is similar to the quasi-static yield stress of unconstrained Ti. This similarity in the constrained and the unconstrained flow stress of Ti can be attributed to the extensive cracking in the Al_3Ti layers adjoining the Ti layers, as seen in Figs 12, 14, 15 and 17. Figure 19 shows that unconstrained Ti yields at ~650 MPa and has a UTS of ~850 MPa. Thus, an average value of 750 MPa was used for σ_C for all the samples. Table 3

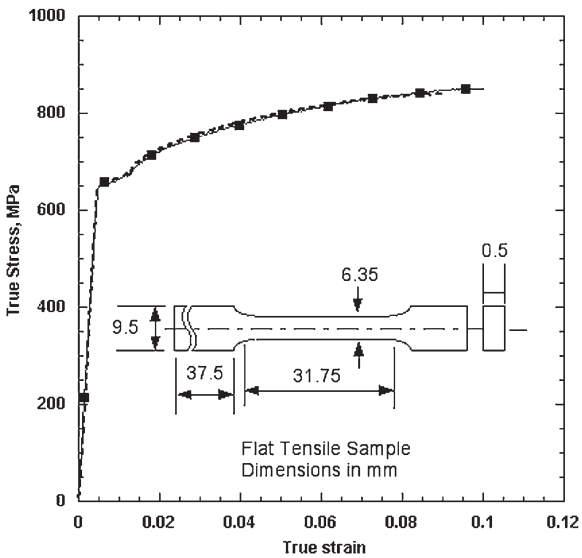

Fig. 19. Quasi-static tensile stress–strain curves of unconstrained Ti–3–2.5 at a strain rate of 10^{-3}/s.

lists the parameters used for calculating the steady-state toughness of the laminate and compares the calculated values with the observed values of the steady-state toughness.

In the divider orientation, the 20Ti predicted K_{SS} value is 91 MPa√m, which is slightly greater than the experimental value of ~80 MPa√m. The predicted value of K_{SS} for the 35Ti sample is 105 MPa√m, somewhat lower than the experimental value of ~115 MPa√m. Both the 20Ti and 35Ti specimens appear to approach steady-state toughness values at the end of the test. In the 14Ti divider sample, the crack redirection occurred at a toughness of ~75 MPa√m, very close to the predicted steady-state toughness of 76 MPa√m.

3.5. Property maps

Figure 20 plots the specific fracture toughness vs. the specific modulus of the composites listed in Table 1 as well as various other engineering materials. The laminates listed in Table 1 are identified as the light gray region in Fig. 20. It can be seen that the Ti–Al_3Ti laminate composites have higher specific toughness than other laminate systems and the Ti–Al_3Ti specific modulus is surpassed only by the metal–Al_2O_3 system. Relative to the best candidate (γ-TiAl/TiNb) amongst the laminates in Table 1, MIL composites have a higher specific fracture toughness and a higher specific modulus for the same volume fraction of the ductile phase. Further, relative to the various metal–Al_2O_3 systems, the MIL composites have a higher specific fracture toughness for the same volume fraction of the ductile phase. While stress–strain data of other laminate systems (Table 1) are not available for comparison, Figs 3 and 5 show that the compressive strength of Ti–Al_3Ti exceeds 1 GPa (depending upon the strain rate and the testing orientation). Thus, owing to the ease of fabrication of Ti–Al_3Ti laminates, low fabrication costs, and their attractive mechanical properties (Figs 3, 5, 7, and 20), the Ti–Al_3Ti laminate system is an excellent candidate for engineering applications

Table 3
Resistance-curve initiation toughness (K_0) and calculated and experimental steady-state toughness

Sample	Young's modulus E (GPa)	Constrained yield stress, σ_C(MPa)	$2r$ (μm)	K_0 (MPa√m)	Metal volume fraction f	Calculated steady state fracture toughness K_{SS} (MPa√m)	Experimental steady state fracture toughness K_{SS} (MPa√m)
14Ti Arrester	200	750	540	15	0.14	77	–
14Ti Divider	200	750	540	7	0.14	76	–
20Ti Arrester	195	750	440	23	0.20	83	–
20Ti Divider	195	750	440	42	0.20	91	80
35Ti Arrester	180	750	300	29	0.35	89	–
35Ti Divider	180	750	300	62	0.35	105	115

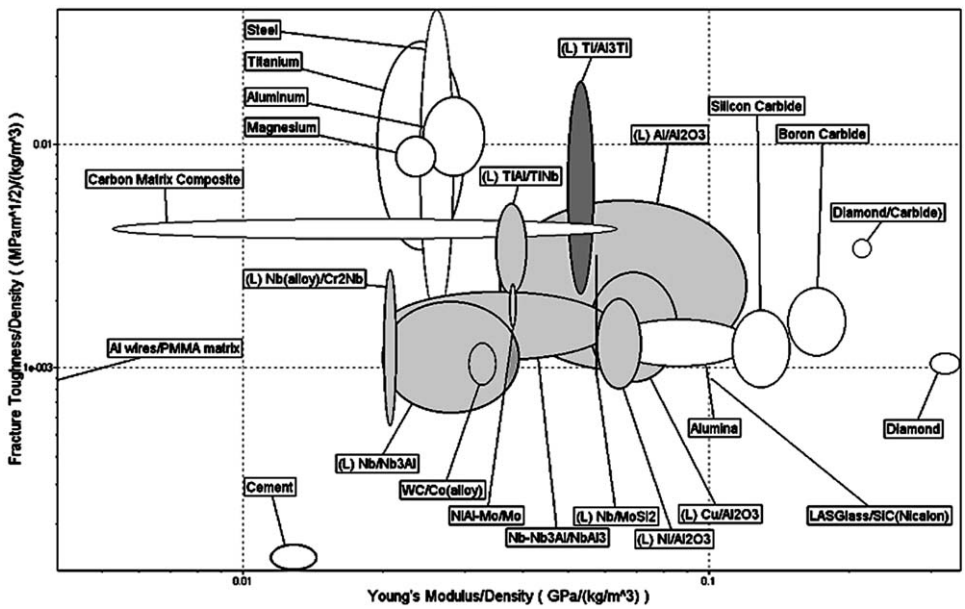

Fig. 20. Property map of Ti–Al_3Ti laminates (dark gray colored) and other laminate systems (identified by (L) and colored in light gray), metals, alloys and composites, showing specific fracture toughness as a function of specific Young's modulus. Data plotted using Cambridge Engineering Selector V3.1 software.

requiring a combination of low density, high strength, high toughness and high stiffness.

4. Summary and conclusions

The fracture and R-curve behavior of Ti–Al_3Ti MIL composites, produced by a one-step process, was investigated using three volume fractions of Ti—14, 20, and 35 percent. The compressive strength, fracture toughness and modulus of the Ti–Al_3Ti composites was compared to other ductile–brittle laminate systems in the literature. The main conclusions are:

1. In the arrester orientation, complete R-curves could only be constructed for the 14Ti volume fraction samples and not for the 20Ti and 35Ti samples since a single, dominant crack could not be grown along the initial notch direction in the latter two compositions. Instead, the crack in the 20Ti and 35Ti samples propagated perpendicular to the initial notch direction, several layers above the initial notch.
2. The initiation toughness in the arrester configuration increases with increasing Ti volume fraction; the values being 7, 23 and 29 MPa$\sqrt{m}$ for 14Ti, 20Ti, and 35Ti, respectively.
3. The R-curve for 14Ti sample in arrester configuration is concave upward indicating the occurrence of geometry dependent large-scale bridging. The bridging zone was estimated to be 3 mm or 6 mm, based on the main cracks originating at the notch or the occurrence of cracks in all the intermetallic layers, respectively.
4. In the arrester orientation, shear bands are formed by cracks blunted in the Ti layer, and serve as nucleation sites for further crack growth in the Al_3Ti layer on the opposite side. The fracture of Ti layers occurred by plastic deformation and necking.
5. In the divider orientation, it was possible to construct R-curves for all volume fractions. The initiation toughness increased with volume fraction from 7 to 42 to 62 MPa$\sqrt{m}$ for 14Ti, 20Ti, and 35Ti. The 20Ti and 35Ti samples reached steady state toughness values of 80 and 115

MPa√m, respectively, that correlated well with the predicted steady-state toughness values of 91 MPa√m and 105 MPa√m, respectively.

6. In the volume fractions tested in the divider orientation, the Ti fractured by microvoid coalescence and the intermetallic by brittle fracture. Toughening of the composites occurs by crack deflection, crack bridging (resulting in R-curve behavior), stress redistribution, and crack front convolution.
7. The Ti–Al_3Ti laminate system offers an excellent combination of specific strength, toughness and stiffness for structural applications.

Acknowledgements

Financial support from the Army Research Office under Contract No. DAAH04-96-1-0376 for the work in this investigation is gratefully acknowledged. The authors would also like to acknowledge the assistance of J. Meissner in sample fabrication and in plotting property maps.

References

[1] Harach DJ, Vecchio KS. Metallurgical and Materials Transactions 2001;32A:1493.
[2] Sauthoff G. Intermetallics. Weinheim, Federal Republic of Germany: VCH Publishers, 1995.
[3] Varin RA, Zbroniec L, Czujko T, Song Y-K. Materials Science and Engineering 2001;A300:1.
[4] Bannister M, Ashby MF. Acta Metallurgica et Materialia 1991;39:2575.
[5] Deve HE, Maloney MJ. Acta Metallurgica et Materialia 1991;39:2275.
[6] Sigl LS, Mataga PA, Dalgleish BJ, McMeeking RM, Evans AG. Acta Metallurgica 1988;36:945.
[7] Mataga PA. Acta Metallurgica 1989;37:3349.
[8] Rao KTV, Soboyejo WO, Ritchie RO. Metallurgical Transactions 1992;23A:2249.
[9] Ashby MF, Blunt FJ, Bannister M. Acta Metallurgica 1989;37:1847.
[10] Cao HC, Dalgleish BJ, Deve HE, Elliott C, Evans AG, Mehrabian R, Odette GR. Acta Metallurgica 1989;37:2969.
[11] Zok F, Hom CL. Acta Metallurgica et Materialia 1990;38:1895.
[12] Flinn BD, Lo CS, Zok FW, Evans AG. Journal of the American Ceramic Society 1993;76:369.
[13] Dalgleish BJ, Trumble KP, Evans AG. Acta Metallurgica 1989;37:1923.
[14] Deve HE, Evans AG, Odette GR, Mehrabian R, Emiliani ML, Hecht RJ. Acta Metallurgica et Materialia 1990;38:1491.
[15] Rao KTV, Odette GR, Ritchie RO. Acta Metallurgica et Materialia 1992;40:353.
[16] Shaw MC, Marshall DB, Dadkhah MS, Evans AG. Acta Metallurgica et Materialia 1993;41:3311.
[17] Heathcote J, Odette GR, Lucas GE, Rowe RG, Skelly DW. Acta Materialia 1996;44:4289.
[18] Bloyer DR, Rao KTV, Ritchie RO. Materials Science and Engineering 1996;A216:80.
[19] Cao HC, Evans AG. Acta Metallurgica et Materialia 1991;39:2997.
[20] Soboyejo WO, Ye F, Chen L-C, Bahtishi N, Schwartz DS, Lederich RJ. Acta Materialia 1996;44:2027.
[21] Leichter HL. Journal of Spacecraft 1966;3:1113.
[22] Odette GR, Chao BL, Sheckherd JW, Lucas GE. Acta Metallurgica et Materialia 1992;40:2381.
[23] Hwu KL, Derby B. Acta Materialia 1999;47:545.
[24] Hansen J, Paige J, Turner P. Effect of thermomechanical processing on the ballisitic performance of titanium. In: Froes FH, Allen PG, Niinomi M, editors. Non-Aerospace Applications of Titanium. Warrendale, PA: The Minerals, Metals & Materials Society; 1998. p. 273.
[25] Kosaka Y, Daggett M, Bristow B. The effect of welded microstructure on ballistic properties of Ti–6Al–4V plates. In: Froes FH, Allen PG, Niinomi M, editors. Non-Aerospace Applications of Titanium. Warrendale, PA: The Minerals, Metals & Materials Society; 1998. p. 281.
[26] Wells MGH, Roopchand B. Titanium applications and R& D for army ground systems. In: Froes FH, Allen PG, Niinomi M, editors. Non-Aerospace Applications of Titanium. Warrendale, PA: The Minerals, Metals & Materials Society; 1998. p. 289.
[27] Fanning JC. Effectiveness of TIMETAL15-3 as armor against small arms (rifles). In: Froes FH, Allen PG, Niinomi M, editors. Non-Aerospace Applications of Titanium. Warrendale, PA: The Minerals, Metals & Materials Society; 1998. p. 297.
[28] Rawers JC, Hansen JS, Alman DE, Hawk JA. Journal of Materials Science Letters 1994;13:1357.
[29] Alman DE, Rawers JC, Hawk JA. Metallurgical and Materials Transactions 1995;26A:589.
[30] Alman DE, Dogan CP, Hawk JA, Rawers JC. Materials Science and Engineering 1995;A192–A193:624.
[31] Maupin, H.E., Rawers, J.C., Hawk, J.A., In: Proceedings of the 1st International Conference on Advanced Synthesis of Engineered Materials, San Francisco, CA, USA, 1992.
[32] Embury JD, Petch NJ, Wraith AE, Wright ES. Transactions of the Metallurgical Society of AIME 1967;239:114.
[33] Lesuer DR, Syn CK, Sherby OD, Wadsworth J, Lewandowski JJ, Hunt WH. J. International Materials Review 1996;41:169.

[34] Bloyer DR, Rao KTV, Ritchie RO. Metallurgical and Materials Transactions 1998;29A:2483.
[35] Hertzberg RW. Deformation and Fracture Mechanics of Engineering Materials, 4th ed. New York: John Wiley and Sons, Inc, 1996.
[36] Harvey KP, Vecchio KS. Unpublished results.
[37] Lu L, Kim YS, Gokhale AB, Abbaschian R. Materials Research Society Symposium Proceedings 1990;194:79.
[38] Sigl LS, Fischmeister HF. Acta Metallurgica 1988;36:887.
[39] Subramanian PR, Mendiratta MG, Miracle DB, Dimiduk DM. Materials Research Society Symposium Proceedings 1990;194:147.
[40] Shalaby SW, May P. Engineered Materials Handbook-Engineering Plastics. Metals Park, OH: ASM International, 1988.
[41] Hertzberg RW. Deformation and Fracture Mechanics of Engineering Materials, 4th ed. New York: Wiley, 1996.
[42] Gilp BF, Desai PD. Properties of Intermetallic Alloys II. Silicides. West Lafayette, IN: Metals Information Analysis Center, 1994.
[43] Lide DR. (ed.) CRC Handbook of Chemistry and Physics, 4.141, Boca Raton, US: CRC Press, 1994.
[44] Metals Handbook—Properties and Selection: Nonferrous Alloys and Pure Metals. Metals Park, OH: American Society for Metals, 1979, p.726.
[45] Metals Handbook—Properties and Selection: Nonferrous Alloys and Pure Metals. Metals Park, OH: American Society for Metals, 1979, p.105.
[46] Metals Handbook—Properties and Selection: Nonferrous Alloys and Pure Metals. Metals Park, OH: American Society for Metals, 1979, p.774.
[47] Lide DR. (ed.) CRC Handbook of Chemistry and Physics. Boca Raton, FL: CRC Press, 1994, pp. 15–39.
[48] Bacalski, C. Personal communications, COI-Ceramics, San Diego, 2002.
[49] Tosdale, J. Outlook Newsletter, 1999;6.
[50] Payne JE, Desai PD. Properties of Intermetallic Alloys I. Aluminides. West Lafayette, IN: Metals Information Analysis Center, 1994.
[51] Dudley RD, Desai PD. Properties of Intermetallic Alloys III. Beryllides and Miscellaneous Intermetallic Alloys. West Lafayette, IN: Metals Information Analysis Center, 1995.
[52] Schneibel JH, Becher PF, Horton JA. Journal of Materials Research 1988;3:1272.
[53] Sauthoff G. Intermetallics. Weinheim, New York: VCH Publishers, 1995.